U.P.B. Sci. Bull., Series B, Vol. 88, Iss.2, 2026 ISSN 1454-2331

# SYNTHESIS, STRUCTURAL EVOLUTION AND IN VITRO BIOACTIVITY OF MAGNETITE-DOPED BIOACTIVE GLASS

Marian RAȘCOV[1], Angela SPOIALĂ[1,2,3], Ludmila MOTELICA[2,3,4], Roxana Doina TRUȘCĂ[2], Otilia-Ruxandra RĂDĂCINĂ[2], Cristina CHIRCOV[1,2], Vasile-Adrian SURDU[5], Denisa FICAI[2,4,6], Ovidiu-Cristian OPREA[2,4,6], Anton FICAI[1,2,3,4], Ecaterina ANDRONESCU[1,2,4,*] , Claudiu-Ștefan TURCULEȚ[7,8]

*A bioactive glass with the composition of 25$SiO_2$-33CaO-33$Na_2O$-3.5$P_2O_5$-5.5$Fe_3O_4$ mol % was synthesized through the sol-gel method. The $Fe_3O_4$-containing bioactive glass was investigated by TG–DSC, XRD, SEM/EDS, FTIR and DLS analyses. After calcination at 350 °C, the material remained mainly amorphous. Weak crystalline contributions related to surface carbonates were evidenced by XRD and consistent with TG–DSC. In vitro bioactivity indicates the typical ion-exchange reactions of bioactive glasses and the formation of a new calcium phosphate layer. DLS indicated the presence of micro-scale aggregates with moderate colloidal stability. The incorporation of $Fe_3O_4$ does not hinder the bioactive response and may introduce additional magnetic functionalities.*

**Keywords**: bioactive glass, $Fe_3O_4$ nanoparticles, sol-gel, in vitro bioactivity, simulated body fluid (SBF).

## 1. Introduction

Recently, bioactive glasses (BGs) have begun to be used more often in tissue regeneration, due to the way they interact with the biological environment. BGs have the capacity to create a strong chemical connection with adjacent biological tissues. This behavior is linked to the progressive formation of a hydroxycarbonate apatite (HCA) layer on their surface when exposed to physiological environments. Since Hench [1] first reported the 45S5 Bioglass® composition, these materials have been the subject of continuous research and are now widely used in bone repair, implant surface modification and tissue engineering [2–4]. The classic bioglass 45S5, with the composition 45$SiO_2$-24.5CaO-24.5$Na_2O$-6$P_2O_5$ (mol%), remains the benchmark due to

---

* Corresponding author, e-mail: ecaterina.andronescu@upb.ro

[1] Department of Science and Engineering of Oxide Materials and Nanomaterials, Faculty of Chemical Engineering and Biotechnologies, NUST POLITEHNICA Bucharest, Romania

[2] National Center for Micro and Nanomaterials, NUST POLITEHNICA Bucharest, Romania

[3] Research Center for Advanced Materials, Products and Processes, NUST POLITEHNICA Bucharest, Romania

[4] Academy of Romanian Scientists, Bucharest, Romania

[5] Department of Materials Science, Faculty of Materials Science and Engineering, "Transilvania" University of Brasov, Romania

[6] Department of Inorganic Chemistry, Physical Chemistry and Electrochemistry, Faculty of Chemical Engineering and Biotechnologies, NUST POLITEHNICA Bucharest, Romania

[7] Faculty of Medicine, Carol Davila University of Medicine and Pharmacy, Bucharest, Romania

[8] Emergency Hospital "Floreasca" Bucharest, Bucharest, Romania

its excellent bioactivity and ion-release characteristics [5,6]. The network dissolution and hydroxyapatite formation are influenced by the high ratio of $CaO:SiO_2$ and the presence of network modifiers such as $Na^+$ and $Ca^{2+}$. This makes the bioglass composition highly reactive and biologically compatible [7]. Although the present composition differs from classical 45S5, the dissolution–precipitation mechanism is expected to follow similar pathways due to the comparable role of $Na_2O$ and CaO as network modifiers.

However, despite these favorable properties, traditional melt-derived glasses remain brittle with limited mechanical reliability, which confines their use to non-structural uses [8-9]. The melt-quenching synthesis method requires high temperatures, usually above 1300 °C. This method generally yields glasses with low specific area and reduced porosity [3,10]. To overcome these limitations, the sol-gel synthesis route has become the most preferred approach for obtaining bioactive glasses with higher surface area, tunable porosity and enhanced bioactivity compared to melt-quenching [11–13]. The sol–gel method offers precise control over the composition of the synthesized materials. This feature facilitates the incorporation of oxides or nanoparticles, thereby enhancing the multifunctional properties of the system [14,15]. Magnetite is among the materials investigated that have become increasingly popular in recent years because it can introduce magnetic character without compromising the bioactive character of glass [16,17].

By integrating magnetite nanoparticles into the structure of bioactive glass, additional functionalities are obtained for bone regeneration, drug delivery and hyperthermia treatments. At the nanoscale level, the magnetite presents superparamagnetic behavior allowing magnetic guidance, localized heating or remotely controlled therapeutic action when exposed to an external magnetic field [18,19]. Iron plays an active role in several vital physiological processes, such as oxygen transport, enzymatic regulation, and cellular metabolism, which together support new tissue formation and angiogenesis [20,21]. Many scientific papers show that introducing the iron into the bioglass composition does not negatively influence the formation of apatite in SBF. Under certain conditions the process of apatite formation is favored and, in addition, gives the bioglass antibacterial and antioxidant properties [22,23].

Studies by Rahman [18] and Hammami [22] showed that a moderate level of iron increases surface reactivity without affecting biocompatibility. The inclusion of magnetite ($Fe_3O_4$) in such glass systems can also influence how the network is arranged and how the glass dissolves, which in turn shapes ion release and the surface chemistry of the material. Through these mechanisms calcium-phosphate deposition is promoted, and the glass's ability to form apatite is kept. At the same time, the material gains magnetic and antibacterial functionalities, valuable for bone regeneration and hyperthermia applications [18,22]. In this manner, the release of ions can be more efficiently managed, influencing cellular activity and supporting the early stages of bone-like apatite formation. $Fe_3O_4$ nanoparticles contribute to the mechanical strengthening of the glass matrix and may act as reinforcing fillers that improve structural integrity and resistance to deformation, while providing magnetic responsiveness useful for biomedical applications [16,24]. As a result, $Fe_3O_4$-doped bioactive glasses combine both biological and structural advantages, making them excellent candidates for multifunctional implants and scaffolds [16,25,26]. The research studies from the last years reveal the fact that such materials could be valuable in applications extending beyond hard tissue engineering. Their porosity supports drug loading and prolonged release of drugs, whereas the magnetic component allows remote activation for healing and controlled therapeutic delivery in soft tissue engineering [4,18,27,28]. The iron oxides can introduce antibacterial properties [22,25,29]. Consequently, magnetite-modified 45S5 glasses are increasingly considered as a new generation of "smart" biomaterials that can respond to external magnetic stimuli while maintaining the inherent bioactivity of the base glass [30-31].

This research paper presents the synthesis of a bioactive glass containing $Fe_3O_4$ nanoparticles through the sol-gel route together with its structural characterization and the evaluation of in vitro bioactivity. The obtained materials were immersed in simulated body fluid (SBF) for 1, 3, 7, 14 and 28 days. The progressive formation of phosphate and silicate phases associated with apatite development was further investigated. This work aims to contribute to the continuous development of multifunctional biomaterials that support bone tissue regeneration while also providing magnetic responsiveness.

## 2. Materials and Methods

### 2.1 Materials

Ferric chloride hexahydrate ($FeCl_3\cdot 6H_2O$, Sigma-Aldrich, 97%) and ferrous chloride tetrahydrate ($FeCl_2\cdot 4H_2O$, Sigma-Aldrich, 98%) were used as iron precursors for magnetite synthesis. The bioglass was prepared from reagent grade powders: tetraethyl orthosilicate (TEOS, Sigma-Aldrich, 98%), calcium nitrate tetrahydrate ($Ca(NO_3)_2\cdot 4H_2O$, Honeywell, 99-103%), sodium carbonate ($Na_2CO_3$, Chimopar, 99.8%), triethyl phosphate (TEP, Sigma-Aldrich, ≥ 99.8%), pluronic P-123 (Sigma-Aldrich), nitric acid ($HNO_3$, Merck, 65%) and absolute ethanol ($C_2H_5OH$, Chimreactiv SRL, 99.9%).

### 2.2. Method of the $Fe_3O_4$ synthesis

Magnetite particles were obtained through co-precipitation method. Briefly, $FeCl_3\cdot 6H_2O$ and $FeCl_2\cdot 4H_2O$ were used as iron ion precursors. The precursors were dissolved in ultrapure water at a molar ratio of 2:1. The obtained solution was slowly added dropwise into a 1M NaOH solution using a peristaltic pump. The obtained precipitate was magnetically separated using a NdFeB magnet placed beneath the reaction beaker. The precipitate was washed with deionized water until neutral pH was reached and dried at room temperature.

### 2.3. Method of the $Fe_3O_4$–doped bioactive glass synthesis

To prepare the $Fe_3O_4$–BG, a sol–gel route was followed. The synthesis began with the preparation of a solution of 500 mL of deionized water, 50 mL of absolute ethanol, and 10 mL of 0.2 N $HNO_3$, into which 5g of Pluronic P123 were added and dissolved. Once the mixture became clear, TEOS was added and the suspension was kept under stirring at room temperature for nearly 2 hours to allow the silica precursor to hydrolyze. After this step, TEP, $Ca(NO_3)_2 \cdot 4H_2O$ and, lastly, $Na_2CO_3$ were added sequentially, each one followed by roughly 45 minutes of mixing.

The $Fe_3O_4$ was then incorporated and the sol was stirred for additional 1 h. Gelation was induced by the gradual addition of a 25% ammonia solution, producing a thick gel that was stirred for 2 more hours. The obtained gel was washed repeatedly with deionized water until neutral pH was reached in order to remove residual soluble inorganic species and weakly adsorbed surfactant molecules. The washed gel was further dried at 60 °C and subsequently calcined at 350 °C for 4 hours to remove the organic template (Pluronic P123), yielding the final $Fe_3O_4$–BG powder. The synthesis protocol was adapted from Ur Rahman et al. [18], with minor adjustments. In Table 1 molar composition of the $Fe_3O_4$–doped bioactive glass is presented.

*Table 1*

**Molar composition of the $Fe_3O_4$–doped bioactive glass**

| Component | $SiO_2$ | CaO | $Na_2O$ | $P_2O_5$ | $Fe_3O_4$ |
|---|---|---|---|---|---|
| mol% | 25 | 33 | 33 | 3.5 | 5.5 |

### 2.4. Preparation of $Fe_3O_4$–doped bioactive glass with different post-synthesis treatments

For evaluation of structural evolution and surface chemistry of the $Fe_3O_4$–doped bioactive glass under different thermal and chemical conditions, several experimental variants were considered. The as-synthesized material obtained after gelation and drying at 60 °C, without subsequent calcination, was denoted as BG_uncalcined. This sample retains the organic template (Pluronic P123) and residual precursor-derived species. The final $Fe_3O_4$–BG powder obtained according to the synthesis protocol described in Section 2.3 corresponds to the material calcined in air at 350 °C for 4 h and was denoted as BG_350C. This reference sample was employed for subsequent physicochemical and in vitro bioactivity investigations. The calcination treatment was selected to promote thermal decomposition of the organic template while preserving the structural characteristics of the glass matrix and the incorporated magnetite phase. To investigate the presence and possible removal of surface carbonate species identified by XRD analysis, a part of the BG_350C sample was treated with 2% (v/v) acetic acid solution for 1 min, followed by thorough rinsing with deionized water and drying. The sample treated with acetic acid solution was labeled BG_350C_AcOH. The structural modifications induced by these post-synthesis treatments were evaluated by TG-DSC and XRD analyses, as appropriate.

### 2.5. Characterization Methods

### 2.5.1. Thermogravimetric analysis (TG-DSC)

Thermal analysis (TG-DSC) of the $Fe_3O_4$-doped bioactive glass samples was performed to investigate their thermal behavior, organic removal and phase stability.

The measurements were carried out using a Netzsch STA 449C Jupiter instrument. The samples were placed in an open crucible made of alumina and heated from room temperature to 900 °C at a constant rate of 10 K·min$^{-1}$, under a dynamic air flow (50 mL·min$^{-1}$). An empty alumina crucible was used as reference. The analysis aimed to evaluate the removal of residual organic species (Pluronic P123), thermal stability of the glass network and the possible presence of carbonate species.

### 2.5.2. X-ray Diffraction (XRD)

The samples were examined by X-ray diffraction using a MiniFlex 600C instrument (Rigaku, Japan) fitted with Cu Kα source ($\lambda = 1.5406$ Å). The measurements were recorded performed in Bragg-Brentano over the 2θ domain between 10° to 80°, with a step size of 0.01° and a scanning rate of 1° min$^{-1}$. Phase identification was performed by comparison with standard reference data. The average crystallite size was calculated using Scherrer's equation, while the unit cell parameters were determined from the main diffraction reflections using SmartLab Studio II software.

### 2.5.3. Scanning Electron Microscopy (SEM) - Energy Dispersive X-Ray Spectroscopy (EDS)

In order to evaluate their morphology and particle size, the magnetite-doped bioglass powders were observed by SEM. The images were collected using a Quanta Inspect F50 microscope (Thermo Fisher/FEI, Eindhoven, The Netherlands). The instrument includes a field-emission gun that can reach a resolution of about 1.2 nm and is equipped with an energy-dispersive X-ray detector having a MnK resolution of 133 eV. The powder samples were mounted on carbon-coated supports and placed inside the microscope chamber for analysis. SEM micrographs were then taken to observe the morphology, particle size, and the distribution of atoms in the surface, together with other microstructural details of the material. When relevant, the images were also used to examine how hydroxyapatite was dispersed within the polymer matrix.

### 2.5.4. Fourier-Transform Infrared Spectroscopy (FTIR)

To identify the specific functional groups and molecular interactions across the synthesized materials, FTIR-ATR was used. All evaluations relied on Bruker Invenio-R spectrometer equipped with a diamond crystal module and an RT-DLaTGS detector. Operating parameters were set at 4 cm$^{-1}$ resolution and 128 scans. Data collection wavenumber range varied slightly by material type. The pristine $Fe_3O_4$ powder was scanned across the 4000-400 cm$^{-1}$ interval, whereas the magnetic bioactive glasses were assessed between 4000-600 cm$^{-1}$.

Spectral data were processed in OPUS software (Bruker). To isolate the true material response, analysts first applied atmospheric compensation alongside standard baseline correction. Vector normalization immediately followed. The conclusive identification of distinct absorption peaks was then carried out entirely by hand, avoiding automated assignment routines.

### 2.5.5. Dynamic Light Scattering (DLS) and Zeta Potential

For DLS analysis, a DelsaMax Pro instrument (Beckman Coulter, Brea, CA, USA) was used. A small quantity of magnetite-doped bioactive glass powder was dispersed in distilled water using an ultrasonic bath for 10 min to obtain a concentration of 1 mg/mL. Immediately after sonication, an aliquot of the suspension was placed into the instrument's measurement cell. Each suspension was analyzed three times consecutively under the same working conditions to ensure data reproducibility.

#### 2.5.6. *In Vitro* Bioactivity Evaluation

*In vitro* tests were performed by immersion of the samples in simulated body fluid (SBF). SBF was prepared according to the Kokubo [32] recipe, which reproduces the ionic balance of human plasma. About 0.5 g of each sample was placed in a polypropylene container with 150 mL of SBF and kept closed during the experiment. The containers were maintained at 36 ± 1 °C for different periods, from 1 to 28 days. While the samples were soaking, the pH and electrical conductivity of the solution were measured from time to time to follow how the ionic exchange evolved. At the end of each immersion time, the material was recovered from the solution, gently washed to remove excess SBF, and then investigated by FTIR and SEM. In this way, the appearance of the eventual apatite layer and the evolution of the surface were monitored.

## 3. Results and Discussion

### 3.1. Thermogravimetric analysis (TG-DSC)

The results from thermal analysis for samples BG_uncalcined and BG_350C are presented in Fig. 1.

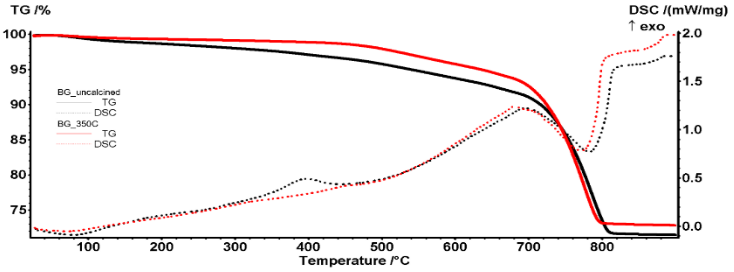

Fig. 1. TG/DSC curves of the $Fe_3O_4$-doped bioactive glass samples in the RT–900 °C range.

The samples exhibit similar TG and DSC curves but with subtle differences originating from the previous thermal treatment of sample BG_350C. The main mass losses values are presented in Table 2.

*Table 2*

**Principal mass losses for samples BG_uncalcined and BG_350C**

| Sample | RT-180 °C (%) | 180-450 °C (%) | 450-680 °C (%) | 680-900 °C (%) | Residual mass at 900 °C (%) |
|---|---|---|---|---|---|
| BG_uncalcined | 1.14 | 2.22 | 4.75 | 20.32 | 71.43 |
| BG_350C | 0.50 | 0.73 | 4.90 | 20.86 | 72.81 |

It can be observed that, as expected, the untreated sample BG_uncalcined exhibits a larger mass loss overall, up to ~700 °C, with ~2%, indicating the amount of substance eliminated in the previous calcination treatment of BG_350C. In the case of calcined sample, elimination of some residual water molecules and even organic surfactant was achieved during the previous thermal treatment [33].

The presence of the small exothermic effect at 397.2 °C on the DSC curve only for uncalcined sample indicates that the thermal treatment, even if carried at a lower temperature of 350 °C, succeeded to remove the organic part due to prolonging calcination time. The absence of this exothermic effect for sample BG_350C suggests the absence of organics in this case. After 450 °C, the remaining nitrate precursors start to decompose, leading to the formation of the corresponding metallic oxides and Nox species, accompanied by a mass loss of 4.75%-4.90% (especially $Ca(NO_3)_2$ will be decomposed up to 600 °C) [34].

Additionally during organic phase removal, partial transformation of nitrates into carbonates can occur, therefore the large mass loss after 700 °C is generated by the decomposition of inorganic salts, mainly calcium carbonate, sodium carbonate and sodium nitrate [35]. This process is accompanied by a strong endothermic effect, with minima at 783.9 °C for BG_uncalcined and 772.4 °C for BG_350C. The relatively high mass loss associated with carbonate decomposition is attributed to extensive surface carbonation rather than bulk crystallization of $CaCO_3$ within the glass matrix. The high CaO content combined with the large specific surface area of sol–gel-derived glasses promote rapid reaction with atmospheric $CO_2$ during drying and storage, according to the reaction $CaO + CO_2 \rightarrow CaCO_3$. Such surface carbonation is frequently reported for Ca-rich bioactive glasses prepared by sol–gel methods and does not reflect structural crystallization of the silicate network. The residual mass at 900 °C is approximately 71–73% for both samples, indicating that the pronounced high-temperature mass loss is mainly associated with the decomposition of carbonate species identified by XRD.

### 3.2. X-ray Diffraction (XRD)

The XRD analysis was used to identify the presence of crystalline phases in the synthesized $Fe_3O_4$ and the $Fe_3O_4$-doped bioactive glass samples. In Fig. 2 is shown a diffraction pattern which presents characteristic reflections of $Fe_3O_4$ with a cubic inverse spinel structure ($Fd\bar{3}m$ space group).

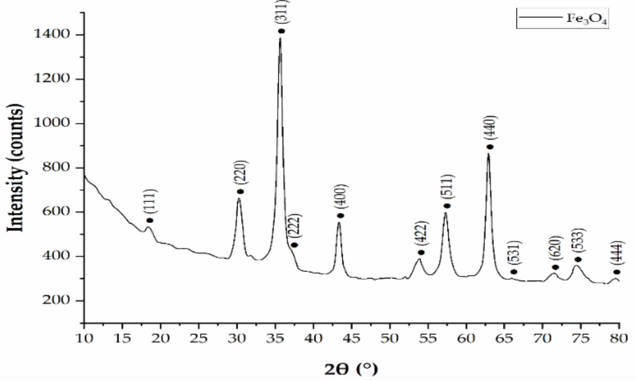

Fig. 2. X-ray diffraction profile of the synthesized pristine magnetite with indexed Miller indices.

The most intense peak appears at 35.6° and corresponds to (311) crystallographic plane. In addition, all reflections are well-defined and consistent with standard reference data for $Fe_3O_4$. No additional peaks corresponding to secondary iron oxide phases were detected. The moderate broadening of the diffraction peaks suggests a nanocrystalline character. The unit cell parameters and the average crystallite size were estimated using the Scherrer equation applied to the main (311) reflection and are presented in Table 3.

*Table 3*

**Structural parameters of pristine $Fe_3O_4$ nanoparticles determined by XRD**

| Sample | Unit cell parameters | | Average crystallite size (nm) |
|---|---|---|---|
| | a = b = c [Å] | a = b = g [˚] | |
| Pristine $Fe_3O_4$ | 8.39 | 90 | 10.3 ± 1.5 |

As shown in Fig. 3, significant structural differences are observed as a function of the treatment.

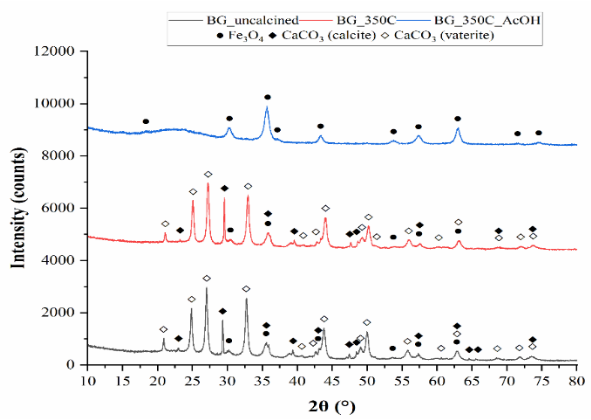

Fig. 3. XRD patterns of BG_uncalcined, BG_350C and BG_350C_AcOH.

BG_uncalcined presents sharp $CaCO_3$ reflections (calcite and vaterite), due to carbonation of the Ca-rich sol–gel matrix. Reflections associated with $Fe_3O_4$ crystalline phase are detectable, confirming that $Fe_3O_4$ remains crystalline after the incorporation into the glass matrix. Calcite and vaterite presence are confirmed in XRD pattern of BG_350C sample. Calcination at 350 °C does not completely remove the carbonate species. The $Fe_3O_4$ peaks are still present, suggesting that the structure remains preserved. According to the diffractogram of BG_350C_AcOH, the washing treatment with diluted acetic acid is effective due to the elimination of $CaCO_3$ peaks. The $Fe_3O_4$ reflections are more pronounced after treatment, indicating that the acid removes carbonate species while preserving the magnetite structure.

For this sample, a broad halo appeared in the XRD profile. The halo found between 20°-25° (2θ) is characteristic of amorphous silicate networks. Thus, the glass matrix is predominantly amorphous despite the presence of surface carbonates. Besides, presence of magnetite phase into obtained materia, XRD results demonstrate that short acid washing after calcination at 350 °C effectively removes surface carbonate species without affecting the crystalline $Fe_3O_4$ phase. The carbonate species are predominantly located at the surface and are chemically accessible.

### 3.3. Scanning Electron Microscopy (SEM) - Energy Dispersive X-Ray Spectroscopy (EDS)

SEM analysis of the bioglass samples prior to immersion in SBF shows a smooth surface without visible crystalline structures, which is characteristic of non-crystalline materials. Small irregularities to the grinding process and sample preparation can be attributed. In Fig. 4 the SEM images of magnetite-doped bioglass samples are presented. The SEM images were recorded at different magnifications and images at proper magnifications were selected to highlight the specific features. After 1 day in SBF immersion, fine-grained deposits, randomly dispersed on the glass surface are observed. These formations indicate the initiation of the ion exchange process between the glass and the aqueous medium, namely the release of $Na^+$ and $Ca^{2+}$ ions from the vitreous network and their replacement by protons ($H^+$). The deposits represent the first nuclei of a phase rich in calcium and phosphate. After 3 days, the number and size of these formations increase significantly, and the surface shows areas partially covered by particle agglomerations. This distribution indicates that the nucleation is already advanced and the apatite layer is beginning to growth.

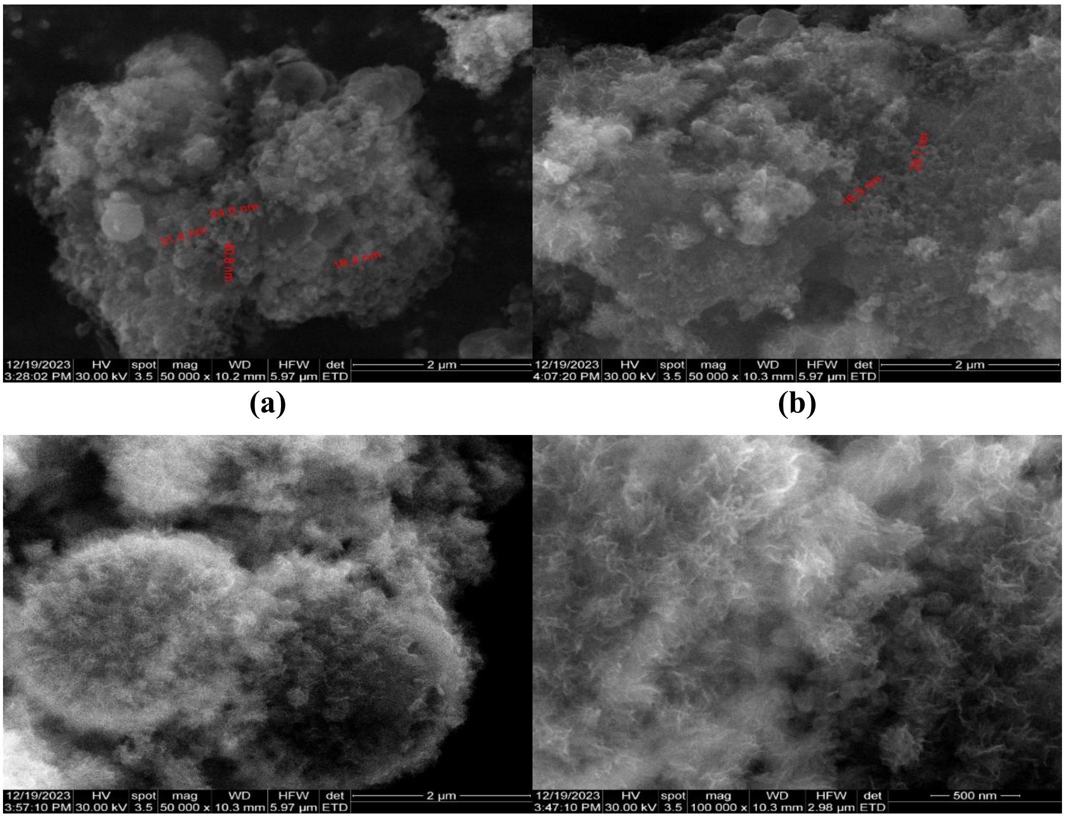

**(a)** **(b)**

**(c)** **(d)**

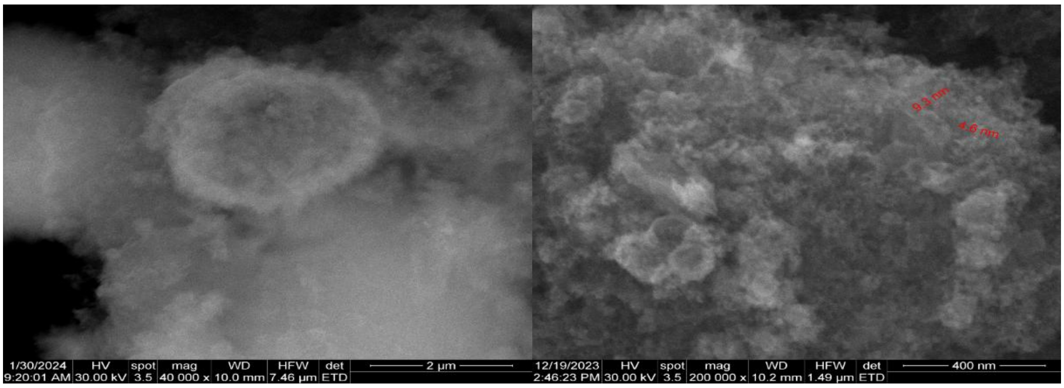

**(e)** **(f)**

Fig. 4. SEM images of bioglass samples: before (a) and after immersion in SBF for 1 day (b), 3 days (c), 7 days (d), 14 days (e) and 28 days (f).

After 1 week of SBF immersion, the surface becomes significantly rougher and is covered by a continuous layer formed by compactly arranged spherical aggregates. This morphology is characteristic of the hydroxyapatite growth stage, during which the previously formed nuclei enlarge and merge, leading to the development of a porous and interconnected coating. After 14 days, the glass surface is almost completely covered by the newly formed layer. The structure has a granular, “cauliflower” like appearance, typical of carbonate hydroxyapatite deposits generated by bioactive materials in contact with simulated fluids. After 28 days, the surface is completely covered by a dense and compact layer of apatite phase, as also evidenced by the FTIR-ATR results discussed later. Individual particles are no longer distinct, a sign of coalescence and maturation of the layer. The presence of the apatite layer proves that the synthesized bioglass is highly bioactive and has the ability to form hydroxyapatite when is immersed in SBF for long time. So, based on the SEM images, it can conclude that these materials are highly active and this is why, at intermediate immersion time, important morphological changes occurred until a mainly apatite coating is deposited.

The particles formed on the glass surface display nanometric dimensions, ranging from approximately 5 to 41 nm. Such small sizes indicate that the apatite phase is composed of fine crystallites associated with the nucleation stage of calcium–phosphate formation. This behavior indicates a progressive development of a Ca-P layer on the glass surface. Their progressive aggregation with increasing immersion time suggests the gradual development of a continuous calcium–phosphate layer on the surface.

In Fig. 5, the EDS profile of the samples is illustrated. The EDS mapping confirms the homogeneous atomic distribution of Si, Ca, O, and P within the glass structure prior to SBF immersion. In the EDS map of the unimmersed sample, several areas where the Fe signal appears are distinguished, compatible with the existence of $Fe_3O_4$ in the glass. The magnetite is not distributed uniformly, but appears in small and scattered portions, not as a continuous phase. Sodium is not visible in the EDS maps because it was not selected for mapping during the measurement.

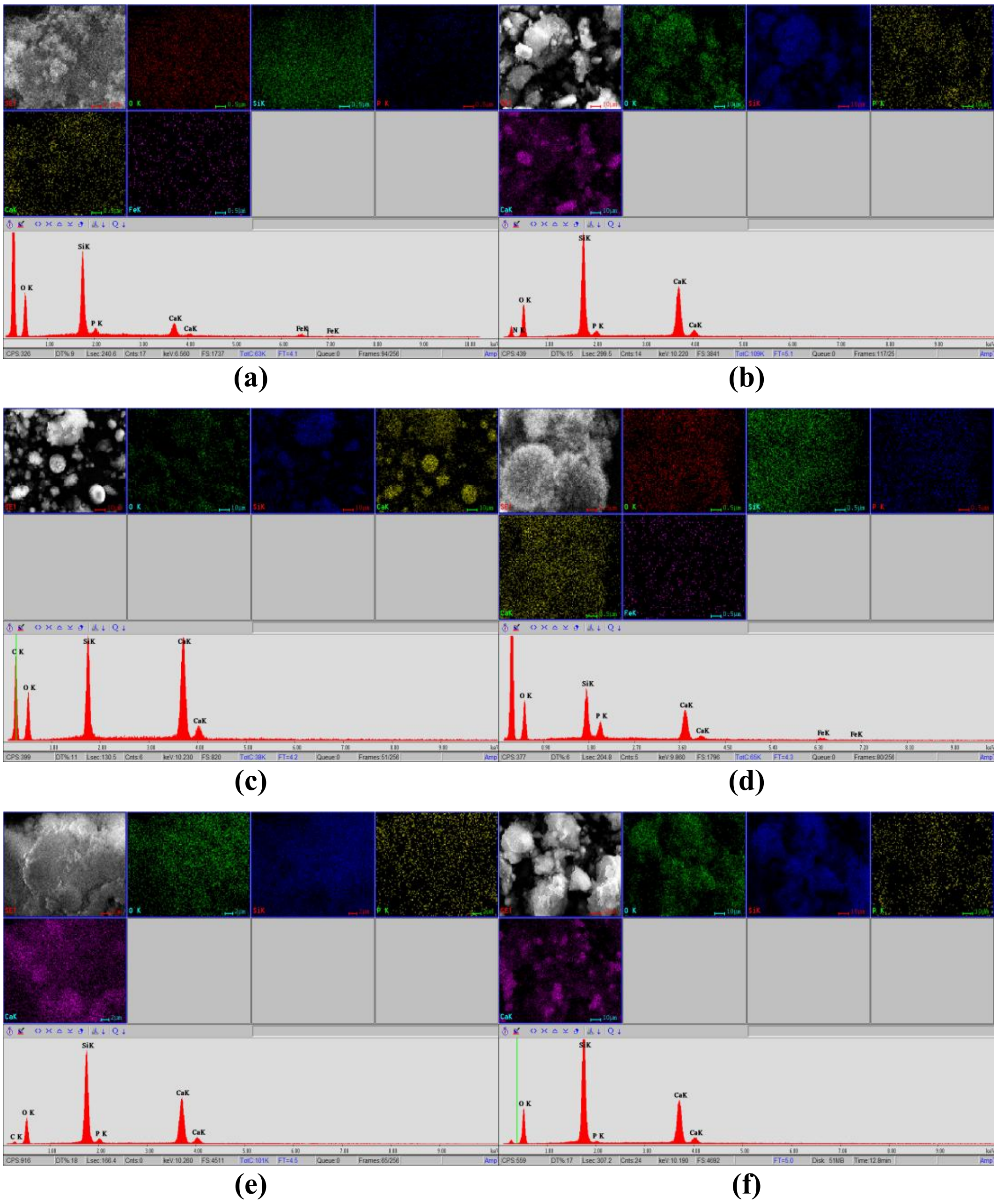

Fig. 5. EDS elemental mapping of bioglass samples: before (a) and after immersion in SBF for 1 day (b), 3 days (c), 7 days (d), 14 days (e) and 28 days (f).

Sodium is part of the glass formulation and is released during the initial ion-exchange stage. After only 24 hours of SBF immersion, EDS maps indicate the appearance of calcium and phosphorous areas, a sign of the initiation of calcium phosphate nucleation. A diminution of the Si signal intensity occurs is observed. That indicates the beginning of surface dissolution and formation of a silica-poor layer. Fe is no longer detectable in the mapped areas, which demonstrates that even the earliest Ca–P deposits already begin to mask the underlying magnetite-containing glass. The behavior is consistent with the leaching of mobile ions from the glass network, while Fe is rapidly covered by the newly formed calcium phosphate layer. After 3 days, Ca-rich agglomerates become more pronounced and are more broadly distributed, whereas both Si and Fe remain strongly suppressed. The distribution of Ca and P suggests the appearance of a discontinuous calcium-phosphate layer, not a compact film.

Over the 7–14 day period, the signals of the two elements become much stronger and expand until they cover almost the entire surface. Si becomes faint across the mapped regions, confirming that the reaction layer thickens sufficiently to screen the underlying glass. Fe remains undetectable in surface maps due to full coverage by the newly formed Ca–P phase. Although the surface is not yet perfectly uniform at 7 days, the 14-day sample exhibits a nearly continuous layer. After 28 days of immersion, the Ca and P distributions are essentially continuous, while the Si signal is almost entirely suppressed in the mapped regions. This demonstrates the formation of a mature, consolidated carbonated hydroxyapatite layer characteristic of highly bioactive glasses. Fe remains absent at the surface, fully masked by the thick Ca–P coating.

Overall, the EDS observations confirm the classical dissolution–precipitation mechanism of bioactive silicate glasses. The enrichment in Ca and P, simultaneous depletion of Si at the surface, and the disappearance of Fe from the accessible interaction volume all indicate progressive apatite growth. The absence of Na in maps is attributed to the lack of Na channel acquisition in mapping and the intrinsic limitations of EDS for light elements.

### 3.4. Fourier-Transform Infrared Spectroscopy (FTIR)

In order to study the vibrational features of the synthesized magnetite, FTIR-ATR spectroscopy was employed. The corresponding spectrum is presented in Fig. 6. The IR spectrum presents characteristic bands in the 400-650 $cm^{-1}$ region corresponding to Fe-O stretching vibrations of the spinel structure. The Fe–O bands are associated with iron ions located in both tetrahedral and octahedral sites of the crystal lattice. The absorption bands observed at 438 $cm^{-1}$ (octahedral sites of magnetite), 535 $cm^{-1}$ (tetrahedral sites of magnetite), 623 $cm^{-1}$ and 683 $cm^{-1}$ are characteristic of Fe-O stretching in magnetite [36–39]. In addition, the band at 1632 $cm^{-1}$ is attributed to the bending vibration of H-O-H from adsorbed water [40].

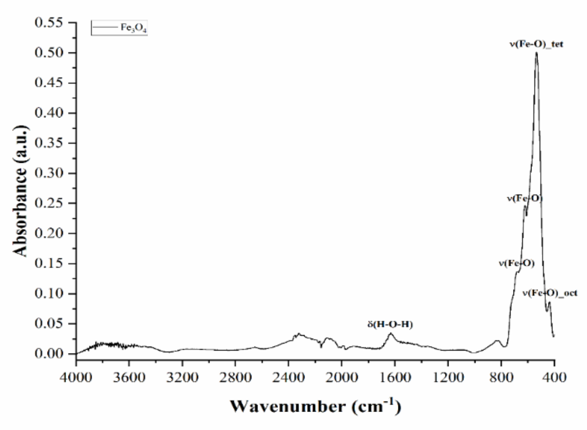

Fig. 6. FTIR-ATR spectra of pristine magnetite in 4000-400 cm$^{-1}$ wavenumber range

The evolution of the FTIR-ATR spectra of the magnetite-doped bioactive glass is presented in Fig. 7 and Fig. 8. The FTIR-ATR spectra recorded for the samples immersed in SBF demonstrates the evolution of a reactive silicate surface, through the gradual development of a carbonated hydroxyapatite layer.

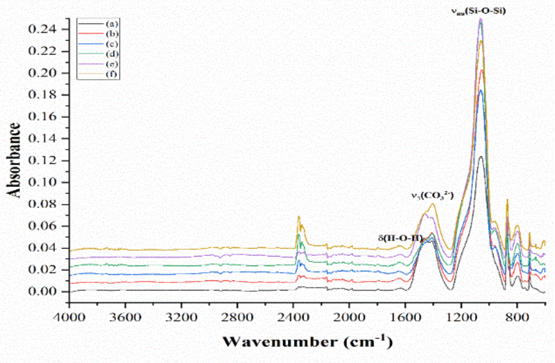

Fig. 7. FTIR-ATR spectra of bioglass samples: before (a) and after immersion in SBF for 1 day (b), 3 days (c), 7 days (d), 14 days (e) and 28 days (f), in 4000-600 cm$^{-1}$ wavenumber range

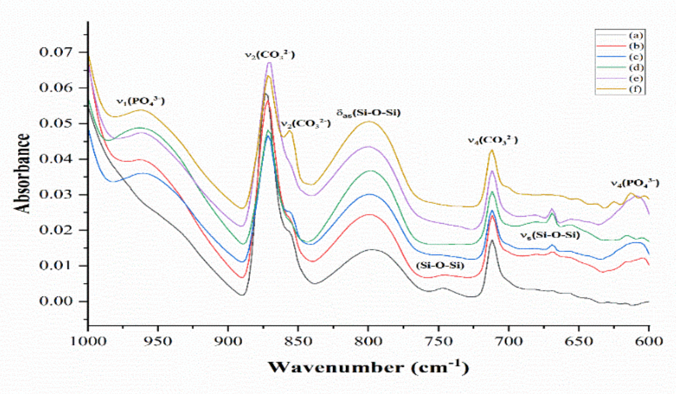

Fig. 8. FTIR-ATR spectra of bioglass samples: before (a) and after immersion in SBF for 1 day (b), 3 days (c), 7 days (d), 14 days (e) and 28 days (f), in 1000-600 cm$^{-1}$ wavenumber range

Phosphate nucleation on the glass surface is confirmed by peaks from the 609 cm$^{-1}$ and 962 cm$^{-1}$, that corresponds to $\nu_4(PO_4^{3-})$ asymmetric bending and $\nu_1(PO_4^{3-})$ symmetric stretching vibrations of phosphate groups [41–44]. The presence of these bands indicates the transition from an initial Si–OH–rich surface to a more stable apatite deposit, a behavior consistently reported for glasses with low Ca/P ratios. The bands at 856 cm$^{-1}$ and 874 cm$^{-1}$ are associated with $\nu_2(CO_3^{2-})$ out-of-plane bending vibration of carbonate groups, whereas the bands at 1406 and 1470 cm$^{-1}$ correspond to $\nu_3(CO_3^{2-})$ asymmetric stretching vibrations [42,45–49]. The peak from 711 cm$^{-1}$ is assigned to $\nu_4(CO_3^{2-})$ in-plane bending vibration, characteristic of carbonate-containing phases [50]. Spectrally, these signals provide a direct match for carbonate species. Their clear detection proves that a carbonated crust successfully precipitates across the glass boundary once exposed to simulated body fluid. Such carbonates may be associated with the formation of carbonated hydroxyapatite or with residual surface carbonates originating from atmospheric carbonation.

The bands observed at 669 cm$^{-1}$, 800 cm$^{-1}$ and 1061 cm$^{-}$1 are characteristics of the silicate network and are assigned to $\nu_s$(Si–O–Si) symmetric stretching, $\delta_{as}$ (Si–O–Si) asymmetric bending and $\nu_{as}$ (Si–O–Si) asymmetric stretching vibrations of Si–O–Si bonds, respectively [41,43,44,51,52]. In addition, a band at 746 cm$^{-1}$ is attributed to a secondary vibrational mode of Si–O–Si bridges, associated with stretching/bending vibrations depending on network polymerization [42,53,54].

Water molecules adsorbed into the porous network generate the distinct $\delta$(H–O–H) bending vibration recorded near 1645 cm$^{-1}$ [55]. The FTIR-ATR datasets establishes the potent bioactive nature of the synthesized glass. The recorded phase evolution drives a highly efficient apatite nucleation sequence, mirroring the traditional behavior expected from functional silicate models.

No distinct absorption bands characteristic of Pluronic P123, such as those at 2970 cm$^{-1}$ assigned to $\nu_{as}(CH_2)$ asymmetric stretching, 2871 cm$^{-1}$ corresponding to $\nu_s(CH_2)$ symmetric stretching and 1343 cm$^{-1}$ attributed to $\delta$(C–H) bending vibrations, were observed in either the uncalcined or calcined sample, suggesting that most of the surfactant was removed during the washing step subsequent thermal treatment [56,57].

### 3.5. Dynamic Light Scattering (DLS) and Zeta Potential

Dynamic Light Scattering was employed to examine how the magnetite-containing bioactive glass behaves once it is dispersed in water. These measurements were performed exclusively on the as-prepared glass powder, prior to immersion in SBF.

The calculation of the hydrodynamic diameter average shows that size is around 2.2 μm, accompanied by a large deviation. Such dimensions clearly point to the presence of sizeable aggregates formed in suspension. This outcome is not unusual for sol–gel-derived bioactive glasses. When the powders are placed in water, their surface quickly absorbs water molecules, and the outer part dissolves slightly. This gives rise to the natural tendency to agglomerate, which explains the large sizes observed.

A zeta potential of approximately −22 mV reinforces the idea that the particles are not very well electrostatically stabilized. A surface charge of this magnitude provides only limited repulsion between particles, which makes the formation of aggregates even more likely. The fact that the polydispersity index (PDI) varies from zero to approximately 0.6 suggests the presence of aggregates of different sizes in the suspension. The average of 0.27 reflects a moderately non-uniform distribution, a common behavior for bioglass which does not affect its reaction processes. Even when present as agglomerates, bioactive glasses continue to exchange ions with the surrounding medium and can initiate the deposition of calcium-phosphate species. In Table 4 the results of DLS analysis of the $Fe_3O_4$–doped bioactive glass sample, prior to immersion in SBF are presented.

*Table 4*

**Results of DLS analysis of the $Fe_3O_4$–doped bioactive glass sample**

| Measurement | Zeta Potential (mV) | Hydrodynamic Diameter (nm) | Polydispersity index (PDI) |
|---|---|---|---|
| 1 | -22.55 | 2569.60 | 0.00 |
| 2 | -22.45 | 1917.00 | 0.24 |
| 3 | -22.82 | 2097.80 | 0.57 |
| Mean ± SD | -22.61 ± 0.19 | 2194.80 ± 336.94 | 0.27 ± 0.29 |

From the way they behave in DLS measurements, it appears that the magnetite-glass particles do not remain separated in water, but rather gather into larger formations, but without completely losing their ability to remain dispersed. The behavior is consistent with what has been reported for similar silicate compositions and agrees with the in vitro results obtained through FTIR, SEM/EDS and SBF immersion experiments.

### 3.6. *In Vitro* Bioactivity Evaluation

At the immersion of the bioglass samples in simulated body fluid, the pH of the solution grows quickly from the starting point of 7.40 to 7.97 in just 24 hours, due to the ion-exchange interactions between the surface of the glasses and the fluid medium. Ions such as $Na^+$ and $Ca^{2+}$ are released into solution, while protons ($H^+$) from the solution interact with the glass network. The process results in partial dissolution of the silicate matrix and the formation of surface -Si-OH groups. For the next 6 days, the pH remains almost constant with small variations indicating that the glass had reached a temporary kinetic equilibrium between the rapid depletion of easily exchangeable $Na^+$ ions and slower diffusion of $Ca^{2+}$ ions from deeper regions of the glass network. This type of behavior can be associated with the migration of heavier or less mobile cations toward the surface. A progressive increase of pH to 8.23 over 28 days was observed. That suggests that a gradual formation of a silica-gel layer followed by the nucleation of a calcium-phosphate phase, whose growth consumes $H^+$ ions from the solution. The increase in pH is in accordance with the formation of the carbonate-substituted hydroxyapatite layer on the glass surface. In Fig. 9, the pH evolution of the samples with soaking time is presented.

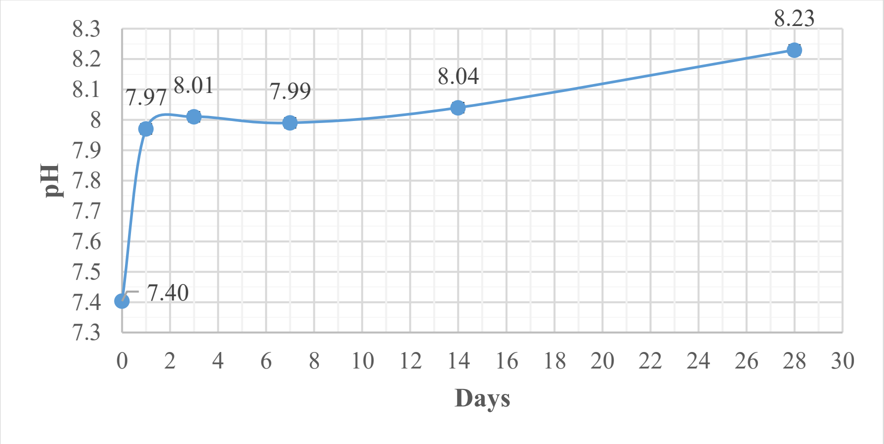

Fig. 9. pH evolution of SBF solution during bioglass soaking time

After a single day of bioglass soaking in SBF medium, the electrical conductivity of the solution is slightly increased. Soluble ions such as $Na^+$ and $Ca^{2+}$ from the bioglass network to the aqueous medium are released. This process results from the ionic exchange between ions from glass structures and protons from solution, leading to an increased total concentration of electrically charged species.

The minor fluctuations of electrical conductivity could be correlated with simultaneous processes of ionic release from the glass and consumption of $Ca^{2+}$ and $PO_4^{3-}$ ions during nucleation of a Ca-P layer on the glass surface. This point represents the beginning of the nucleation and early growth of carbonated hydroxyapatite. After 28 days of immersion in SBF, the conductivity values remain almost unchanged showing that the system has reached a quasi-equilibrium state. This behavior confirms bioactivity and the ability to generate a stable apatite layer at the interface with the SBF solution. The variation of electrical conductivity in SBF with soaking time is presented in Fig. 10.

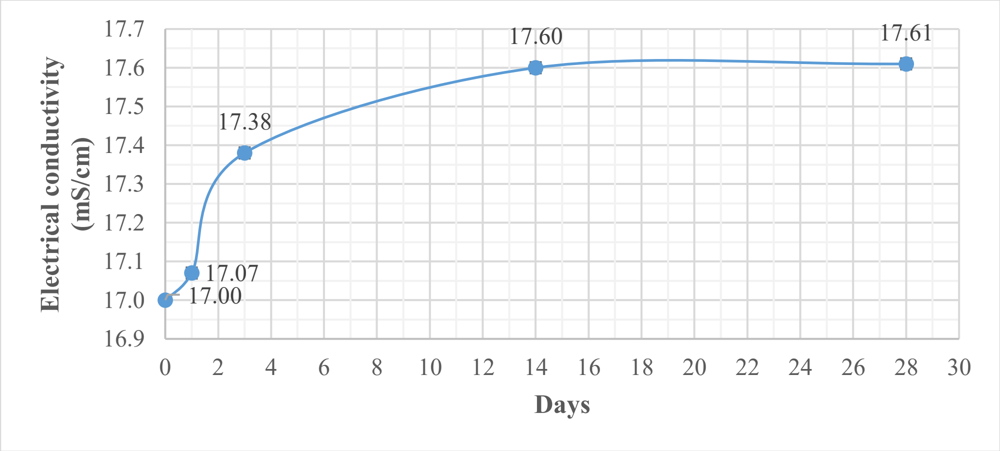

Fig. 10. Electrical conductivity evolution of the SBF solution during bioglass soaking

## 4. Conclusions

Within this work a bioactive glass modified with $Fe_3O_4$ was synthesized and its subsequent structural and in vitro evaluation was done. The main contribution of this work is to demonstrate that the incorporation of magnetite does not significantly alter the predominantly amorphous character of the glass under moderate thermal treatment (350 °C), while the material keeps its ability to generate a stable carbonated hydroxyapatite layer during immersion in SBF. Results obtained from FTIR and SEM/EDS observations, together with pH and conductivity measurements, show that the material undergoes the expected sequence of reactions characteristic of silicate bioactive glasses, eventually forming a compact and adherent apatite layer after 28 days in SBF.

Overall, the behavior of this $Fe_3O_4$–bioactive glass suggests that it could be developed as a multifunctional system for bone repair, maintaining the reactivity of conventional silicate glasses while introducing magnetic features through the incorporated nanoparticles. Such a combination may be of interest for applications ranging from magnetically assisted implant positioning to localized drug release or hyperthermia-based therapeutic strategies.

## Acknowledgment

The authors acknowledge the financial support of the Smart2Graph—Smart nerve grafts based on graphene-related composite materials with electric-triggering capability for central and peripheral nervous system regeneration, funded within the Flag Era Call as well as the national grant of the Ministry of Research, Innovation and Digitization of Romania, CNCS/CCCDI-UEFISCDI, project number 28/17.05.2024 is also highly acknowledged. The authors are grateful to the Romanian Government for providing access to the research infrastructure of the National Center for Micro and Nanomaterials through the National Program titled “Installations and Strategic Objectives of National Interest”.

## REFERENCES

[1]. *L.L. Hench*, "Bioceramics: From Concept to Clinic." *Journal of the American Ceramic Society*, **74**, (7), 1991, 1487–1510.

[2]. *L.L. Hench*; *J.M. Polak*, "Third-Generation Biomedical Materials." *Science*, **295**, (5557), 2002, 1014–1017.

[3]. *J.R. Jones*, "Reprint of: Review of bioactive glass: From Hench to hybrids." *Acta Biomaterialia*, **23**, 2015, S53–S82.

[4]. *Y. Zhu*; *X. Zhang*; *G. Chang*; *S. Deng*; *H.F. Chan*, "Bioactive Glass in Tissue Regeneration: Unveiling Recent Advances in Regenerative Strategies and Applications." *Advanced Materials*, **37**, (2), 2025, 2312964.

[5]. *M.N. Rahaman*; *D.E. Day*; *B. Sonny Bal*; *Q. Fu*; *S.B. Jung*; *L.F. Bonewald*; *A.P. Tomsia*, "Bioactive glass in tissue engineering." *Acta Biomaterialia*, **7**, (6), 2011, 2355–2373.

[6]. *L.L. Hench*, "The story of Bioglass®." *Journal of Materials Science: Materials in Medicine*, **17**, (11), 2006, 967–978.

[7]. *K. Łukowicz*; *B. Zagrajczuk*; *A. Nowak*; *Ł. Niedźwiedzki*; *M. Laczka*; *K. Cholewa-Kowalska*; *A.M. Osyczka*, "The role of CaO/SiO2 ratio and P2O5 content in gel-derived bioactive glass-polymer composites in the modulation of their bioactivity and osteoinductivity in human BMSCs." *Materials Science and Engineering: C*, **109**, 2020, 110535.

[8]. *R. Sergi*; *D. Bellucci*; *V. Cannillo*, "A Review of Bioactive Glass/Natural Polymer Composites: State of the Art." *Materials*, **13**, (23), 2020, 5560.

[9]. *G. Kaur*; *V. Kumar*; *F. Baino*; *J.C. Mauro*; *G. Pickrell*; *I. Evans*; *O. Bretcanu*, "Mechanical properties of bioactive glasses, ceramics, glass-ceramics and composites: State-of-the-art review and future challenges." *Materials Science and Engineering: C*, **104**, 2019, 109895.

[10]. *R. Li*; *A.E. Clark*; *L.L. Hench*, "An investigation of bioactive glass powders by sol-gel processing." *Journal of Applied Biomaterials*, **2**, (4), 1991, 231–239.

[11]. *C. Wu*; *J. Chang*, "Mesoporous bioactive glasses: structure characteristics, drug/growth factor delivery and bone regeneration application." *Interface Focus*, **2**, (3), 2012, 292–306.

[12]. *D. Arcos*; *M. Vallet-Regí*, "Sol–gel silica-based biomaterials and bone tissue regeneration." *Acta Biomaterialia*, **6**, (8), 2010, 2874–2888.

[13]. *K. Deshmukh*; *T. Kovářík*; *T. Křenek*; *D. Docheva*; *T. Stich*; *J. Pola*, "Recent advances and future perspectives of sol–gel derived porous bioactive glasses: a review." *RSC Advances*, **10**, (56), 2020, 33782–33835.

[14]. *M. Chen*; *Y. Wang*; *P. Yuan*; *L. Wang*; *X. Li*; *B. Lei*, "Multifunctional bioactive glass nanoparticles: surface–interface decoration and biomedical applications." *Regenerative Biomaterials*, **11**, 2024, rbae110.

[15]. *R. Borges*; *J.S.S. Oliveira*; *A.P. Queiroz*; *T. Zambanini*; *A.M. Hanashiro*; *N.B. Lima*; *J.F. Schneider*; *J. Marchi*, "On the structure of Ag-containing sol-gel bioactive glasses: A surface crystal growth of metallic silver removes its network modifier role in the glass structure." *Open Ceramics*, **16**, 2023, 100449.

[16]. *T.M. Valverde; V.M.R. Dos Santos; P.I.M. Viana; G.M.J. Costa; A.M. De Goes; L.R.D. Sousa; V.F. Xavier; P.M.D.A. Vieira; D. De Lima Silva; R.Z. Domingues; et al.*, "Novel Fe3O4 Nanoparticles with Bioactive Glass–Naproxen Coating: Synthesis, Characterization, and In Vitro Evaluation of Bioactivity." *International Journal of Molecular Sciences*, **25**, (8), 2024, 4270.

[17]. *C. Taşar*; *B. Ercan*, "Fabrication and biological properties of magnetic bioactive glass nanoparticles." *Ceramics International*, **49**, (8), 2023, 12925–12933.

[18]. *M.S. Ur Rahman*; *M.A. Tahir*; *S. Noreen*; *M. Yasir*; *I. Ahmad*; *M.B. Khan*; *K.W. Ali*; *M. Shoaib*; *A. Bahadur*; *S. Iqbal*, "Magnetic mesoporous bioactive glass for synergetic use in bone regeneration, hyperthermia treatment, and controlled drug delivery." *RSC Advances*, **10**, (36), 2020, 21413–21419.

[19]. *R. Borges; L.M. Ferreira; C. Rettori; I.M. Lourenço; A.B. Seabra; F.A. Müller; E.P. Ferraz; M.M. Marques; M. Miola; F. Baino; et al.*, "Superparamagnetic and highly bioactive SPIONS/bioactive glass nanocomposite and its potential application in magnetic hyperthermia." *Biomaterials Advances*, **135**, 2022, 112655.

[20]. *Q. Ru*; *Y. Li*; *L. Chen*; *Y. Wu*; *J. Min*; *F. Wang*, "Iron homeostasis and ferroptosis in human diseases: mechanisms and therapeutic prospects." *Signal Transduction and Targeted Therapy*, **9**, (1), 2024, 271.

[21]. *J. Dürig*; *M. Calcagni*; *J. Buschmann*, "Transition metals in angiogenesis – A narrative review." *Materials Today Bio*, **22**, 2023, 100757.

[22]. *I. Hammami*; *S.K. Jakka*; *I. Sá-Nogueira*; *J.P. Borges*; *M.P.F. Graça*, "The Effect of Iron Oxide Insertion on the In Vitro Bioactivity, and Antibacterial Properties of the 45S5 Bioactive Glass." *Biomimetics*, **9**, (6), 2024, 325.

[23]. *F. Kermani*; *A. Vojdani-Saghir*; *S. Mollazadeh Beidokhti*; *S. Nazarnezhad*; *Z. Mollaei*; *S. Hamzehlou*; *A. El-Fiqi*; *F. Baino*; *S. Kargozar*, "Iron (Fe)-doped mesoporous 45S5 bioactive glasses: Implications for cancer therapy." *Translational Oncology*, **20**, 2022, 101397.

[24]. *C. Vichery*; *J.-M. Nedelec*, "Bioactive Glass Nanoparticles: From Synthesis to Materials Design for Biomedical Applications." *Materials*, **9**, (4), 2016, 288.

[25]. *Y. Jin; H. Liu; L. Chu; J. Yang; X. Li; H. Zhou; H. Jiang; L. Shi; J. Weeks; J. Rainbolt; et al.*, "Initial therapeutic evidence of a borosilicate bioactive glass (BSG) and Fe3O4 magnetic nanoparticle scaffold on implant-associated Staphylococcal aureus bone infection." *Bioactive Materials*, **40**, 2024, 148–167.

[26]. *Z. Sohani*; *H. Jamshidi Aval*; *S.M. Rabiee*, "Bioactive glass and iron oxide nanoparticle composite coatings for Ti-6Al-4V implants: Microstructure, corrosion behavior, bioactivity and cellular response." *Applied Surface Science Advances*, **27**, 2025, 100734.

[27]. *M. Vargas Guerrero*; *F.M.A. Aendekerk*; *C. De Boer*; *J. Geurts*; *J. Lucchesi*; *J.J.C. Arts*, "Bioactive-Glass-Based Materials with Possible Application in Diabetic Wound Healing: A Systematic Review." *International Journal of Molecular Sciences*, **25**, (2), 2024, 1152.

[28]. *R. Sreena*; *G. Raman*; *G. Manivasagam*; *A.J. Nathanael*, "Bioactive glass–polymer nanocomposites: a comprehensive review on unveiling their biomedical applications." *Journal of Materials Chemistry B*, **12**, (44), 2024, 11278–11301.

[29]. *T.M. Tiama*; *H. Elhaes*; *M.A. Ibrahim*; *A. Refaat*; *M.A.M. El-Mansy*; *N.M. Sabry*, "Molecular and biological activities of metal oxide-modified bioactive glass." *Scientific Reports*, **13**, (1), 2023, 10637.

[30]. *A. Batista*; *T.M. Valverde*; *C.C.M. Silva*; *R.M.F. Da Costa E Silva*; *G.M.J. Costa*; *J.D. Fabris*; *J.D. Ardisson*; *J.M.D.F. Ferreira*; *V.M.R. Dos Santos*; *Â.L. Andrade*, "Magnetic core-shell nanocomposites with bioactive glass coatings for hyperthermia-assisted bone cancer therapy." *Magnetic Medicine*, **1**, (3), 2025, 100039.

[31]. *T. Tithito; S. Sillapaprayoon; V. Chantho; W. Pimtong; J. Thongbunchoo; N. Charoenphandhu; N. Krishnamra; N. Yong; A. Lert-itthiporn; W. Maneeprakorn; et al.*, "Evaluation of magnetic hyperthermia, drug delivery and biocompatibility (bone cell adhesion and zebrafish assays) of trace element co-doped hydroxyapatite combined with Mn–Zn ferrite for bone tissue applications." *RSC Advances*, **14**, (40), 2024, 29242–29253.

[32]. *T. Kokubo*; *H. Kushitani*; *S. Sakka*; *T. Kitsugi*; *T. Yamamuro*, "Solutions able to reproduce *in vivo* surface-structure changes in bioactive glass-ceramic A-W$^3$." *Journal of Biomedical Materials Research*, **24**, (6), 1990, 721–734.

[33]. *R. Lavric*; *C. Vreme*; *C. Busuioc*; *G.-O. Isopencu*; *A.-I. Nicoara*; *O.-C. Oprea*; *D.-D. Banciu*; *I. Constantinoiu*; *A.-M.-R. Musat*, "The Effect of Silver and Samarium on the Properties of Bioglass Coatings Produced by Pulsed Laser Deposition and Spin Coating." *Journal of Functional Biomaterials*, **14**, (12), 2023, 560.

[34]. *A. Zhao*; *B. Xiong*; *Y. Han*; *H. Tong*, "Thermal decomposition paths of calcium nitrate tetrahydrate and calcium nitrite." *Thermochimica Acta*, **714**, 2022, 179264.

[35]. *E.S. Freeman*, "The Kinetics of the Thermal Decomposition of Sodium Nitrate and of the Reaction between Sodium Nitrite and Oxygen." *The Journal of Physical Chemistry*, **60**, (11), 1956, 1487–1493.

[36]. *M. Bustamante-Torres*; *D. Romero-Fierro*; *J. Estrella-Nuñez*; *B. Arcentales-Vera*; *E. Chichande-Proaño*; *E. Bucio*, "Polymeric Composite of Magnetite Iron Oxide Nanoparticles and Their Application in Biomedicine: A Review." *Polymers*, **14**, (4), 2022, 752.

[37]. *K. Winiarczyk*; *W. Gac*; *M. Góral-Kowalczyk*; *Z. Surowiec*, "Magnetic properties of iron oxide nanoparticles with a DMSA-modified surface." *Hyperfine Interactions*, **242**, (1), 2021, 48.

[38]. *M. Jebali*; *G. Colangelo*; *L. Haurie*; *I. Bekri-Abbes*; *A.M. Lacasta*, "Thermo-physical properties of paraffin wax with iron oxide nanoparticles as phase change material for heat storage applications." *Journal of Physics: Conference Series*, **2385**, (1), 2022, 012026.

[39]. *V. Swathi Pon Sakthi Sri*; *Y. Aron Santhosh Kumar*; *M. Savurirajan*; *D.K. Jha*; *N.V. Vinithkumar*; *G. Dharani*, "Anticancer efficacy of magnetite nanoparticles synthesized using aqueous extract of brown seaweed Rosenvingea intricata, South Andaman, India." *Scientific Reports*, **14**, (1), 2024, 20255.

[40]. *N.R. Jannah*; *D. Onggo*, "Synthesis of $Fe_3 O_4$ nanoparticles for colour removal of printing ink solution." *Journal of Physics: Conference Series*, **1245**, (1), 2019, 012040.

[41]. *R. Kamalian*; *A. Yazdanpanah*; *F. Moztarzadeh*; *R. Ravarian*; *Z. Moztarzadeh*; *M. Tahmasbi*; *M. Mozafari*, "Synthesis and characterization of bioactive glass/forsterite nanocomposites for bone and dental implants." *Ceramics-Silikáty*, **56**, (4), 2012, 331–340.

[42]. *S.V. Sirkiä*; *M. Nakamura*; *S. Qudsia*; *M. Siekkinen*; *J.-H. Smått*; *J. Peltonen*; *T.J. Heino*; *L. Hupa*; *P.K. Vallittu*, "Structural and elemental characterization of glass and ceramic particles for bone surgery." *Dental Materials*, **37**, (9), 2021, 1350–1357.

[43]. *Y.-Y. Chen*; *T.-L. Ma*; *P.-J. Chang*; *Y.-J. Chiou*; *W.-M. Chang*; *C.-F. Weng*; *C.-Y. Chen*; *Y.-K. Chang*; *C.-K. Lin*, "Synergistic Effect of Strontium Doping and Surfactant Addition in Mesoporous Bioactive Glass for Enhanced Osteogenic Bioactivity and Advanced Bone Regeneration." *Polymers*, **17**, (2), 2025, 187.

[44]. *S.M. Ahmadi*; *A. Behnamghader*; *A. Asefnejaad*, "Sol-gel synthesis, characterization and in vitro evaluation of SiO2−CaO−P2O5 bioactive glass nanoparticles with various CaO/P2O5 ratios." *Digest Journal of Nanomaterials and Biostructures*, **12**, (3), 2017, 847–860.

[45]. *M. Ni*; *B.D. Ratner*, "Differentiating calcium carbonate polymorphs by surface analysis techniques—an XPS and TOF-SIMS study." *Surface and Interface Analysis*, **40**, (10), 2008, 1356–1361.

[46]. *F. Vergnaud*; *X. Kesse*; *A. Jacobs*; *F. Perton*; *S. Begin-Colin*; *D. Mertz*; *S. Descamps*; *C. Vichery*; *J.-M. Nedelec*, "Magnetic bioactive glass nano-heterostructures: a deeper insight into magnetic hyperthermia properties in the scope of bone cancer treatment." *Biomaterials Science*, **10**, (14), 2022, 3993–4007.

[47]. *A. Nawaz*; *S. Bano*; *M. Yasir*; *A. Wadood*; *M.A. Ur Rehman*, "Ag and Mn-doped mesoporous bioactive glass nanoparticles incorporated into the chitosan/gelatin coatings deposited on PEEK/bioactive glass layers for favorable osteogenic differentiation and antibacterial activity." *Materials Advances*, **1**, (5), 2020, 1273–1284.

[48]. *M. Araújo*; *M. Miola*; *G. Baldi*; *J. Perez*; *E. Verné*, "Bioactive Glasses with Low Ca/P Ratio and Enhanced Bioactivity." *Materials*, **9**, (4), 2016, 226.

[49]. *J.R.J. Delben*; *K. Pereira*; *S.L. Oliveira*; *L.D.S. Alencar*; *A.C. Hernandes*; *A.A.S.T. Delben*, "Bioactive glass prepared by sol–gel emulsion." *Journal of Non-Crystalline Solids*, **361**, 2013, 119–123.

[50]. *D.E. Baciu*; *J. Simitzis*, "Synthesis and characterization of acrylic bone cement reinforced with calcium carbonate-bioceramic." *Journal of optoelectronics and advanced materials*, **15**, (3–4), 2013, 145–149.

[51]. *R. Kumar R.*; *S. Ashok Kumar*; *K.P. Bhuvana*, "Preparation and Evaluation of Bioactivity of Porous Bioglass Tablets for Bone Tissue Regeneration." *SciMedicine Journal*, **1**, (3), 2019, 112–123.

[52]. *M. Mami*; *A. Lucas-Girot*; *H. Oudadesse*; *R. Dorbez-Sridi*; *F. Mezahi*; *E. Dietrich*, "Investigation of the surface reactivity of a sol–gel derived glass in the ternary system SiO2–CaO–P2O5." *Applied Surface Science*, **254**, (22), 2008, 7386–7393.

[53]. *I. Jagusa*; *C.M. Gonah*; *A.D. Garkida*,5. Characteristics of Bioactive Glass Produced with Phosphate Rock from Dange in Sokoto State. In *International Journal of Research and Analysis in Science and Engineering*; 2021; Vol. 1, pp. 48–58.

[54]. *S. Borhan*; *S. Hesaraki*; *A.-A. Behnamghader*; *E. Ghasemi*, "Rheological evaluations and in vitro studies of injectable bioactive glass–polycaprolactone–sodium alginate composites." *Journal of Materials Science: Materials in Medicine*, **27**, (9), 2016, 137.

[55]. *C. Scaggion*; *M. Marinato*; *G. Dal Sasso*; *L. Nodari*; *T. Saupe*; *S. Aneli*; *L. Pagani*; *C.L. Scheib*; *M. Rigo*; *G. Artioli*, "A fresh perspective on infrared spectroscopy as a prescreening method for molecular and stable isotopes analyses on ancient human bones." *Scientific Reports*, **14**, (1), 2024, 1028.

[56]. *S. Sunoqrot*; *S. Aliyeh*; *S. Abusulieh*; *D. Sabbah*, "Vitamin E TPGS-Poloxamer Nanoparticles Entrapping a Novel PI3Kα Inhibitor Potentiate Its Activity against Breast Cancer Cell Lines." *Pharmaceutics*, **14**, (9), 2022, 1977.

[57]. *M. Akrami-Hasan-Kohal*; *A. Chouchou*; *S. Blanquer*; *T. Sharkawi*, "Everolimus-encapsulation in Pluronic P123 self-assembled micelles as drug delivery systems for drug-coated balloons." *International Journal of Pharmaceutics: X*, **7**, 2024, 100230.